Theoretical analysis of the moment-curvature relationship of coal gangue concrete beam

Bin Cai[1], Kaiyi Li[1] and Feng Fu[2*]

[1] School of Civil Engineering, Jilin Jianzhu University, Changchun 130118, Jilin, China.

[2] Department of Engineering, School of Science and Technology, City, University of London, London, EC1V, 0HB, United Kingdom

*Correspondence: feng.fu.1@city.ac.uk

Abstract

At present, there are fewer studies on the application of coal gangue concrete to structural components. In order to study the variation of moment-curvature relationship of steel fiber-reinforced coal gangue concrete (SFCGC) beams, a simplified calculation method of moment-curvature is proposed in this study for the calculation of moment-curvature measurements of SFCGC beams. The calculation equations of SFCGC beams were optimized based on current design codes, including theoretical calculations of flexural stiffness, crack width and spacing, cracking moment, and ultimate moment. The calculated results were compared with the experimental results to verify that the cracking moment and ultimate moment of SFCGC beams are slightly lower than those of natural concrete (NC) beams, but the cracking moment, flexural stiffness, and ductility of SFCGC beams can be increased by incorporating steel fibers. And increasing the rebar ratio can significantly improve the load-carrying capacity of SFCGC beams but will reduce the ductility. The calculated value has a small error with the experimental value, which proves that the optimized design specification formula has a high

calculation accuracy and is applicable to the design of the bending behavior of SFCGC beams. This provides a theoretical basis for the subsequent related research.

Keywords: Steel fiber reinforced coal gangue concrete beam; Moment-curvature; Crack width; Cracking moment; Ultimate moment

1. Introduction

Coal gangue is a by-product of coal mining and raw coal processing. The accumulation of its waste significantly threatens the health and safety of the human population, as well as the ecological health of the environment (Gong et al. 2016). To date, approximately 4.5 billion tons of coal gangue waste has been generated from the process of coal mining in China and continues to grow at a rate of 150-200 million tons per year. Meanwhile, however, the large-scale urbanization construction efforts in China have caused the mining rate of natural sand and gravel to exceed the natural recovery rate of these materials. Coal gangue, with its stable structure and low reactivity, needs to be activated via mechanical grinding and thermal and chemical activation methods before it can be used in construction applications (Guo et al. 2016; Li et al. 2013). By testing the basic physical and mechanical properties of coal gangue aggregate, Wang and Zhao (2015) showed that coal gangue can meet the requirements of compressive strength of concrete aggregate. Through the mechanical property test of coal gangue concrete without steel fiber, Zhu et al. (2020) found that when the coal gangue replacement rate is more than 50%, it will lead to a rapid decrease in its compressive strength. Under standard curing conditions, coal gangue addition reduced the early strength of concrete, increased porosity and water absorption, but improved resistance to chloride ions or gas permeability. Using coal gangue instead of gravel to make concrete can simultaneously consume a large amount of coal gangue (Karimaei et al. 2020) and reduce the use of gravel in the construction industry. This method holds a significant impact on the development of eco-friendly building materials and the reduction of industrial energy consumption and ultimately, to protect the natural environment (Wu et al. 2018; Moghadam et al. 2019; Qin et al. 2019). For example, Sun and Li (2011) developed coal gangue concrete for gob-side entry retaining, which not only solve the problem of ecological environment and resource shortage, but also reduce the cost of filling material and increase the economic benefit of coal mine enterprise. Besides, the coal gangue also could be used as inexpensive adsorbent in industrial wastewater pretreatment (Jabłońska et al. 2020). And self- self-ignited gangue can also be recycled as a partial substitute for Portland cement and reduce the carbon footprint of fossil fuels in order to protect the environment (Qin and Gao 2019). In recent years, scholars around the world have conducted extensive experimental and theoretical research on the mechanical properties of coal gangue concrete. Jin-min (2011) found that when the proportion of coal gangue replacement gravel is less than 30%, the working capacity of concrete is relatively stable; with the increasing amount of coal gangue replacement, the working capacity of concrete decreases; with the increasing amount of coal gangue replacement, the apparent density of concrete increases continuously. Guo and Zhu (2011) used orthogonal test and comprehensive balance method to analyze the durability of coal gangue concrete to determine the best ratio of coal gangue concrete. Zhang (2020) found that the addition of spontaneous combustion coal gangue aggregate significantly affects the mechanical properties of concrete, reducing the compressive strength, splitting tensile strength, and elastic modulus. Ma (2020) concluded that the concrete mixed with calcined coal gangue has good sulfate resistance. As coarse aggregate, coal gangue has high compressive strength and durability in alkali-activated coal gangue-slag concrete and can be used in chemical erosion environments such as chloride or sulfate. Gao (2021) proposed constants for predicting the splitting tensile strength and elastic modulus of coal gangue concrete. In addition, Liu

(2020) further proposed a new model to accurately estimate the elastic modulus of spontaneous combustion coal gangue concrete by considering the replacement rate, compressive strength, and density of the concrete. However, there have been relatively few studies on coal gangue components.

Invented in 1874, steel fiber-reinforced concrete has been a useful structural material since the 1970s (Katzer and Domski 2012), as the addition of steel fibers considerably improves the mechanical properties of concrete, including its impact strength, toughness, flexural and tensile strength, ductility, and resistance to cracking and spalling (Mohammadi et al. 2008). Although steel fibers have been increasingly used in structures such as building floors, prefabricated elements, tunnels, heavy-duty pavements, and mining structures (Atis and Karahan 2009, Wang et al. 2020), nonetheless this composite material still requires extensive research (Brandt 2008; Olivito and Zuccarello 2010). The fibers can effectively retard the appearance and development of microcracks in the concrete matrix and help improve the toughness, ductility and bending properties of UHPC and avoid brittle damage (Chen et al. 2019). And the aspect ratio and volume fraction of steel fibers have significant effects on the workability of steel fiber composites (Yazıcı 2007). The aspect ratio is generally between 50 and 100. As the l/d increases, the uneven distribution of fibers in the concrete mix and the probability of flocculation increase. The most suitable volume fraction of steel fibers is 0.5%-2.5% (Yazıcı 2007). The existence of voids in the bond between coal gangue and cement mortar compromises the compressive strength and durability of concrete and has the disadvantages of high porosity and strong water absorption (Ma et al. 2018). Therefore, steel fibers can be added to coal gangue concrete to enhance its performance and increase its suitability for construction.

In the field of theoretical research on the moment-curvature relationship and the calculation of deflection, Wu et al. (2021) developed an iterative algorithm to calculate the deflection of unbonded

FRP tendon prestressed beams. The Babilio and Lenci (2017) study obtained uncoupled linear approximation provides an indication of a more suitable curvature definition. Kwak and Kim (2002) performed a material nonlinear analysis of reinforced concrete beams considering tensile softening branching and bond slip. The control equations describing the bond-slip behavior in the beam are derived, which simplifies the finite element modeling and analysis process and effectively describes the bond-slip behavior. And the developed algorithm is also reflected in the bending moment-curvature relationship of the RC section. Hadhood (2018) established the moment-curvature relationship for full-scale circular FRP-RC members by means of a validated layer-by-layer analytical model. Viet and Zaki (2019) first developed mathematical formulations to predict and describe the internal material structure of the composite considering the solid phase transition of SMA bars. Then the analytical expression of the bending moment-curvature relationship is obtained. Foroughi and Yüksel (2020) obtained the moment-curvature relationship of reinforced concrete square columns in SAP2000 software by considering the nonlinear properties of the material. Priestley et al. (1971) derived the bending moment relationship for prestressed concrete members using a purely analytical approach, including the effect of concrete tension between cracks. Hasan et al. (2019) developed a numerical integration method to study moment-curvature behavior of circular normal strength concrete (NSC) and high strength concrete (HSC) columns reinforced with (GFRP) rods.

Concrete with coal gangue as coarse aggregate can turn waste into treasure, resolve the problem of environmental pollution caused by the accumulation of coal gangue, and improve economic and ecological benefits, which is in line with the concept of national sustainable development. Flexural performance is an important characteristic of reinforced concrete members. For the theoretical calculation of the flexural performance of concrete beams in this aspect of research, Du et al. (Du et al. 2021) carried out a theoretical analysis of the flexural performance of alkali-activated concrete beams. And Jia et al. (Jia et al. 2021) carried out a theoretical analysis of the flexural performance of concrete beams with the coarse aggregate post-filling process. But at present, there is no relevant theoretical analysis of the flexural performance of steel fiber reinforced gangue concrete beam, which has brought inconvenience to the application of engineering structural designers. In this paper, based on the four-point bending test of SFCGC beams, with coal gangue replacement rate, steel fiber volume content (SFVC), rebar ratio, and beam height as the parameter variables, the curvature, the cracking moment, ultimate bending moment, flexural stiffness and crack spacing and width of SFCGC beams are theoretically analyzed. The flexural performance of the SFCGC beams was investigated and verified using the current structural code, demonstrating the applicability of the current provisions to the design of SFCGC beams. The test results and findings provide theoretical support for the popularization and application of coal gangue.

2. Test Materials

2.1. Materials

The appearance of the coal gangue is shown in Fig. 1(a). The chemical composition of coal gangue was determined by X-ray fluorescence spectroscopy (XRF) completed at Jilin University. The results are shown in Table 1. As shown in Table 1, the contents of SiO_2 and Al_2O_3 in coal gangue are higher, 48.14% and 16.48%, respectively. Si and Al are the main components of coal gangue chemical composition, and the change of its structure level in the activation process is the key to affecting the strength of coal gangue composite cement. It is known that coal gangue can be used as concrete coarse aggregate (Li et al. 2006). Corrugated steel fibers were used, as shown in Fig. 1(b). By the physical property test performed at Jilin Jianzhu University, the specific physical properties of the raw materials used to prepare SFCGC specimens are shown in Table 2.

(a) Coal gangue (b) Steel fiber

Fig. 1. Appearance of the materials.

Table 1

Chemical composition of the coal gangue.

SiO_2	Al_2O_3	Fe_2O_3	FeO	BaO	MgO	K_2O	Na_2O	TiO_2	P_2O_5	MnO
48.14	16.48	4.59	7.03	7.40	6.53	2.16	3.70	2.31	0.51	0.2

Table 2

Materials for the experimental study.

Materials	Information
Cement	P.O42.5 ordinary Portland cement of Changchun Cement Co., Ltd; initial setting time: 90min; final setting time: 265min; compressive strength: 24.9Mpa(3days) and 48.7Mpa(28days); specific surface area: 344m^2/kg; loss on ignition: 2.6%
Sand	River sand; the fineness modulus: 2.8; and the bulk density: 1450kg/m^3
Stone	Ordinary gravel; size gradation: 5–25mm; bulk density: 1500kg/m^3; and crushing

	index:7%
Coal gangue	Size gradation: 5–25mm; bulk density: 1206kg/m^3; water absorption: 8.3%; and crushing index: 18%
Water	Ordinary tap water
Plasticizer	The rate of water reduction: 20%; fineness: 0.315mm, and the major component: Sodium β-Naphthalene Sulfonate
Steel fiber	Undulated steel fiber (Fig. 1(b)), 38mm long, 1mm wide, and 0.35-0.5mm thick, aspect ratio: 50, and density: 7850kg/m^3

2.2. SFCGC mixtures

Six mixing ratios were used for experimental testing, as shown in Table 3. The first and second numerals in the designation of each specimen denote the coal gangue replacement rate (0%, 50%, 100%) and the SFVC (0%, 0.5%, 1%, 1.5%), respectively. The dimensions and quantities of coal gangue specimens were determined according to the provisions given by GB/T 50081-2019 (CABR 2019). Specifically, three test blocks of each with a dimension of 150 mm × 150 mm × 150 mm and one test block with a dimension of 100 mm × 100 mm × 300 mm were cast for each mixing ratio. Uniaxial compression and splitting tensile tests were performed using a Type YAR-2000 electrohydraulic servo universal testing equipment in accordance with GT50081-2019 (CABR 2019) as shown in Fig. 2(a)-(b), similar equipment can be seen in Fu (2010,2018), Gao (2017) ,Qian (2022,2020),The cube axial compressive strength (f_{cu}) and splitting tensile strength (f_t) of concrete were obtained from these two tests respectively. And the axial compressive strength of prisms (f_c) and the concrete modulus of elasticity of concrete (E_c) is obtained by uniaxial compression testing of prisms as shown in Fig. 2(c). The results provide data to support the subsequent theoretical analysis, as shown in Table 3.

(a) Cubic axial compression resistance test (b) Cube splitting tensile test (c) Prismatic axial compression test

Fig. 2. Test setup for mechanical properties of concrete.

Table 3

Mixture compositions. Unit:kg/m^3

No.	R%	V_{sf}%	Cg	gravel	cement	sand	Pl	W/C	f_{cu}/Mpa	f_c/Mpa	f_t/Mpa	E_c/Gpa
M0-1	0	1	0	1155.5	503.7	622.22	5.04	0.40	47.11	36.23	3.53	34.05
M50-1	50	1	577.7	577.8	503.7	622.22	5.04	0.40	46.62	35.45	3.51	33.96
M100-0	100	0	1155.5	0	503.7	622.22	5.04	0.40	35.87	25.67	2.44	29.79
M100-0.5	100	0.5	1155.5	0	503.7	622.22	5.04	0.40	42.31	32.39	2.88	33.11
M100-1	100	1	1155.5	0	503.7	622.22	5.04	0.40	46.56	34.58	3.48	33.95
M100-1.5	100	1.5	1155.5	0	503.7	622.22	5.04	0.40	46.83	34.81	3.61	34.02
M100-2	100	2	1155.5	0	503.7	622.22	5.04	0.40	46.82	34.69	3.62	34.00

Note: R = the coal gangue replacement rate; V_{sf} = the SFVC, CG = the coal gangue coarse aggregate; Pl = the plasticizer; W/C = the water-cement ratio.

2.3. SFCGC preparation

In accordance with the provisions given by GB/T 50080-2002 (CABR 2003), Qiant(2020,2021), the concrete specimens were prepared using a mortar stone wrapping method with a dry–wet mixing process (Gao 2017). Fig. 3 shows the process of making the specimens.

Fig. 3. The specimen fabrication process.

2.4. Specimen parameters

To investigate the influence of R, V_{sf}, and ρ on the moment-curvature relationship of SFCGC beams, a total of ten SFCGC beams and two natural concrete (NC) beams were designed. The specific parameters of the experimental beams are shown in Table 4. The concrete cover of each specimen had a thickness of 25 mm. The detailing and cross-sections of the beams refer to Cai's tests (Cai et al. 2023), and the basic properties of the rebar used in the specimens obtained from Cai’s tests (Cai et al. 2023).

Table 4

Design of the test beams.

Specimens	b/mm	h/mm	h_0/mm	L/mm	L_0/mm	R%	V_{sf}%	ρ%
N2-0-1	150	200	175	2000	1800	0	1	1.17
S1-100-1	150	200	175	2000	1800	100	1	0.6

S2-100-1	150	200	175	2000	1800	100	1	1.17
S3-100-1	150	200	175	2000	1800	100	1	1.94
S2-50-1	150	200	175	2000	1800	50	1	1.17
S2-100-0	150	200	175	2000	1800	100	0	1.17
S2-100-0.5	150	200	175	2000	1800	100	0.5	1.17
S2-100-1.5	150	200	175	2000	1800	100	1.5	1.17
S2-100-2	150	200	175	2000	1800	100	2	1.17
N4-0-1	150	300	275	2000	1800	0	1	1.12
S4-50-1	150	300	275	2000	1800	50	1	1.12
S4-100-1	150	300	275	2000	1800	100	1	1.12

Note: b = beam section width; h = beam section height; h_0 = the effective height; L = beam length; L_0 = beam effective length; ρ = the rebar ratio. In the specimen names, the first symbol indicates the type of materials, S = SFCGC, N = NC; the second symbol indicates ρ; the numeral "1, 2, 3, 4" indicates 0.6%, 1.17%, 1.94%, 1.12%, respectively; the third symbol indicates R; and the forth symbol indicates V_{sf}.

2.5. Test loading Scheme

A 500-kN hydraulic servo pressure testing machine was used in the test. As shown in Fig. 4, a four-point bending test was performed with two-point symmetrical loading. The pure bending region of the beam had a length of 600 mm. According to GB/T 50152-2012 (CABR 2011), force-controlled loading was adopted in this test. Before formal loading, a preload of 5 kN was applied to ensure the normal operation of the equipment. After preloading, the load was zeroed, and formal loading began at a rate of 2 kN/min. At each level, the cumulative load was 5 kN and was held for 5 min, during which crack width was recorded using a crack width gauge. After steel rebar yielding, the load was applied continuously at a reduced rate of 1 kN/min and an increment of 2 kN at each level until specimen failure. To obtain changes in the transverse strain of the concrete, the concrete strain was measured on both sides of the beam: on one side a traditional strain gauge method was used, and on the other side, a DIC technique was used. Digital Image Correlation (DIC) is a non-contact measurement technique that can be used to track the full-field strain and displacement of deforming objects (Schreier et al. 2009). The test system is shown in Fig. 5.

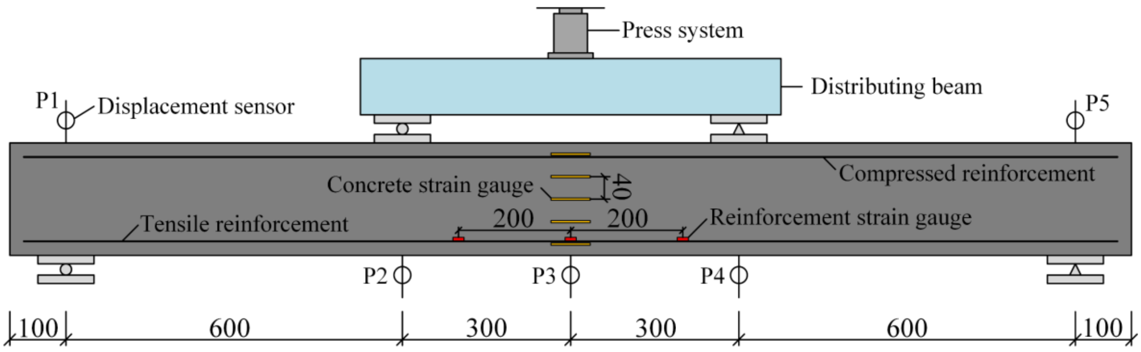

Fig. 4. Test setup of beam specimens.

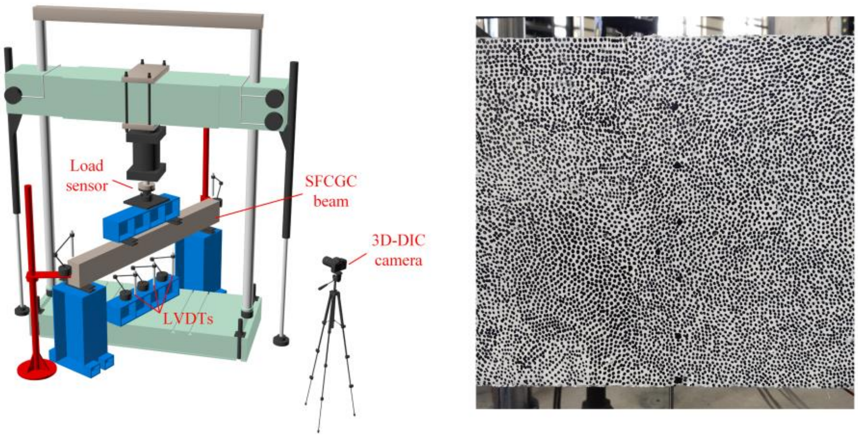

(a) DIC test instrument (b) Beam speckle pattern

Fig. 5. DIC test preparation.

3. Experimental phenomena and results

3.1. Experimental phenomena

The load-mid-span deflection curve (Cai et al. 2023) and crack development pattern (Fig. 6) of the SFCGC beams were similar to those of the NC beams. Some of the data in Fig. 6 are sourced from Cai's study (Cai et al. 2023). When the load reached $0.3F_u$ (where F_u is the ultimate load), 1-3 vertical cracks with a width generally < 0.02 mm initially appeared in the region near the loading point in the pure bending section. Distribution of concrete strains along the height of the specimen is obtained from Cai's study (Cai et al. 2023). When the SFCGC beams cracked, the component's deflection increased. At the same time, the concrete and rebar strain readings changed to some extent. Under all levels of load, the strain of each point on the normal section of concrete in the tension area is approximately proportional to the distance from the point to the neutral axis. Nonetheless, they still met the plane-section assumption. This proves that the SFCGC beam has a stable bending bearing capacity. When the load increased to $0.5F_u$, new cracks in the pure bending section no longer appeared, and the cracks propagated along the direction of the compression zone. Compared with the NC beam, the crack development of the SFCGC beam is faster due to the porous structure of coal gangue aggregate, but the crack development rate of the SFCGC beam can be slowed down by adding steel fiber. At the same time, the deflection of the beam gradually increased. The neutral axis of the beam moved upward, but the crack width did not increase significantly. As the load further increased to 0.8-$0.85F_u$, the rebar yielded, the deflection of the beam specimen increased rapidly, and the cracks continuously extended and widened. Finally, the concrete in the compression zone was crushed, as shown in Fig. 6. No sliding failure occurred at the composite interface of any specimens.

(a) N2-0-1 (b) S1-100-1

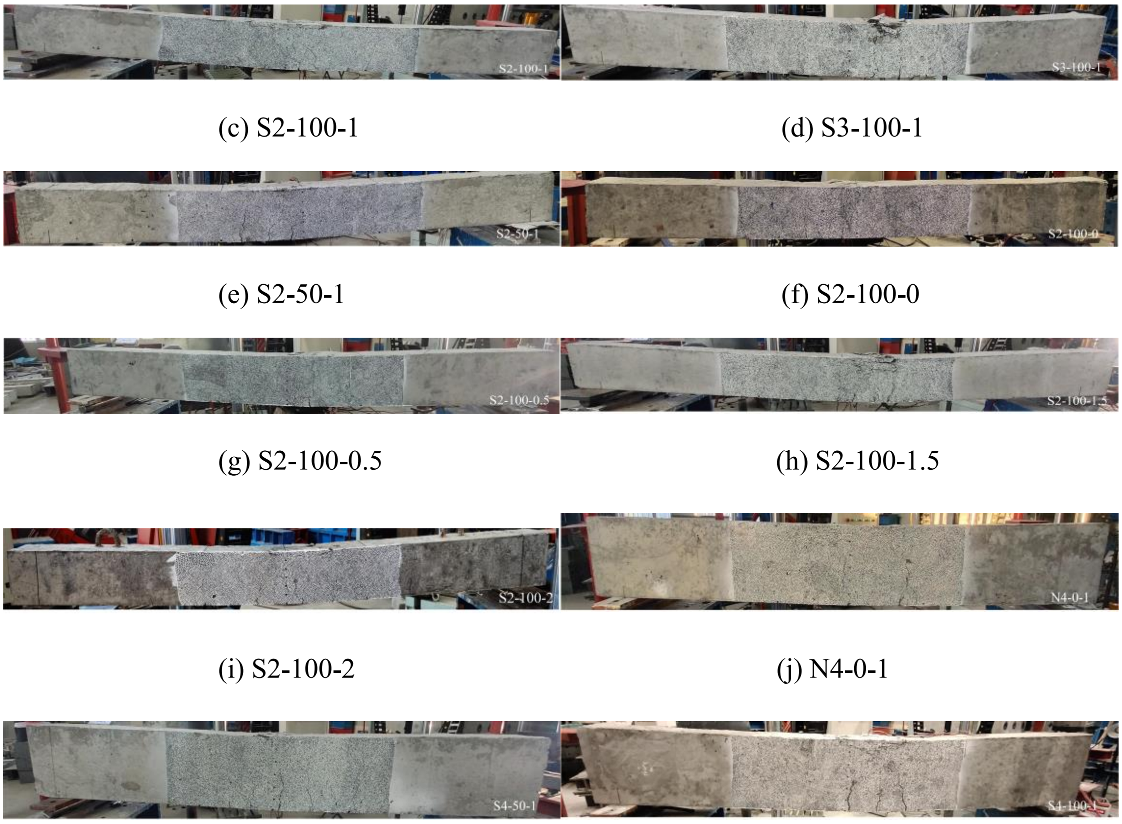

(c) S2-100-1 (d) S3-100-1

(e) S2-50-1 (f) S2-100-0

(g) S2-100-0.5 (h) S2-100-1.5

(i) S2-100-2 (j) N4-0-1

(k) S4-50-1 (l)S4-100-1

Fig. 6. Loaded state of the specimens.

3.2. Strain of longitudinal bars

Fig. 7 demonstrates the moment-rebar strain relationship in the span of the beam specimen. The moment increases gradually as the longitudinal rebar starts to yield. Similar to the moment-curvature relationship, the rebar ratio and beam depth have an important effect on the bending performance. Table 5 compares the yielding moments determined from the moment-curvature relationship and the moment-rebar strain relationship. The ratio of these two results was between 0.96-1.06, indicating that the errors in these two results were small.

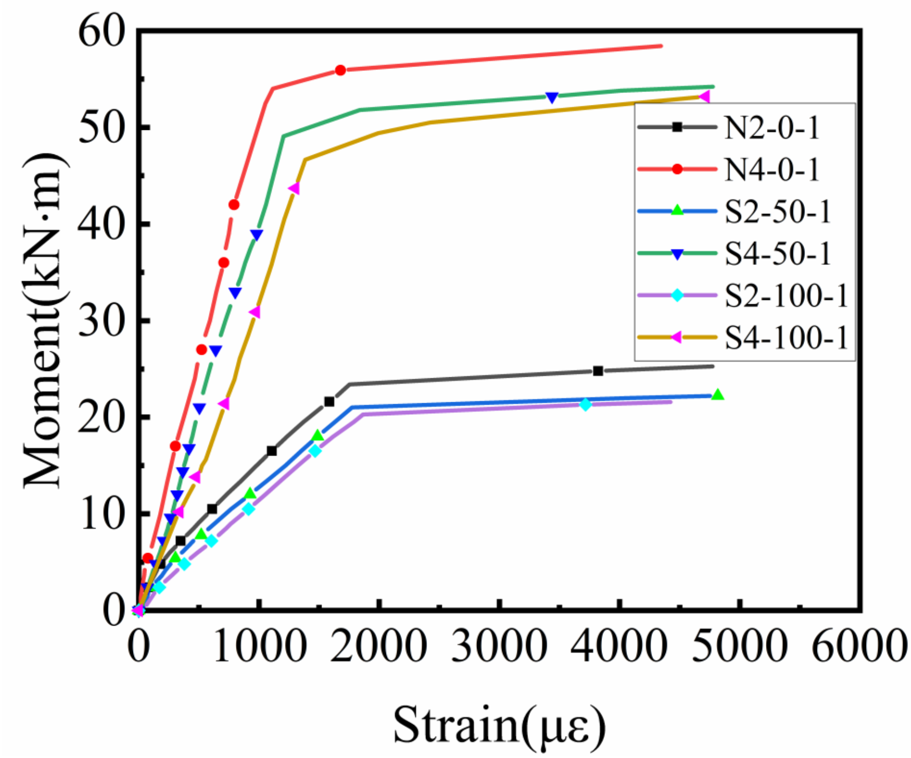

(a) Effect of coal gangue replacement rate on the moment-rebar strain relationships of the beams

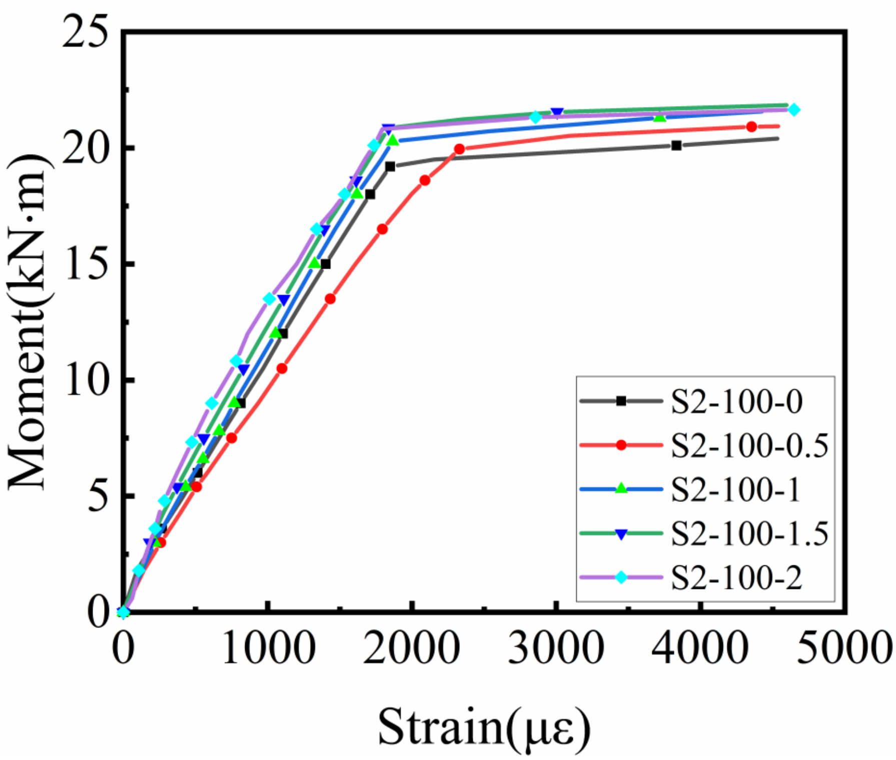

(b) Effect of SFVC on the moment-rebar strain relationships of the beams

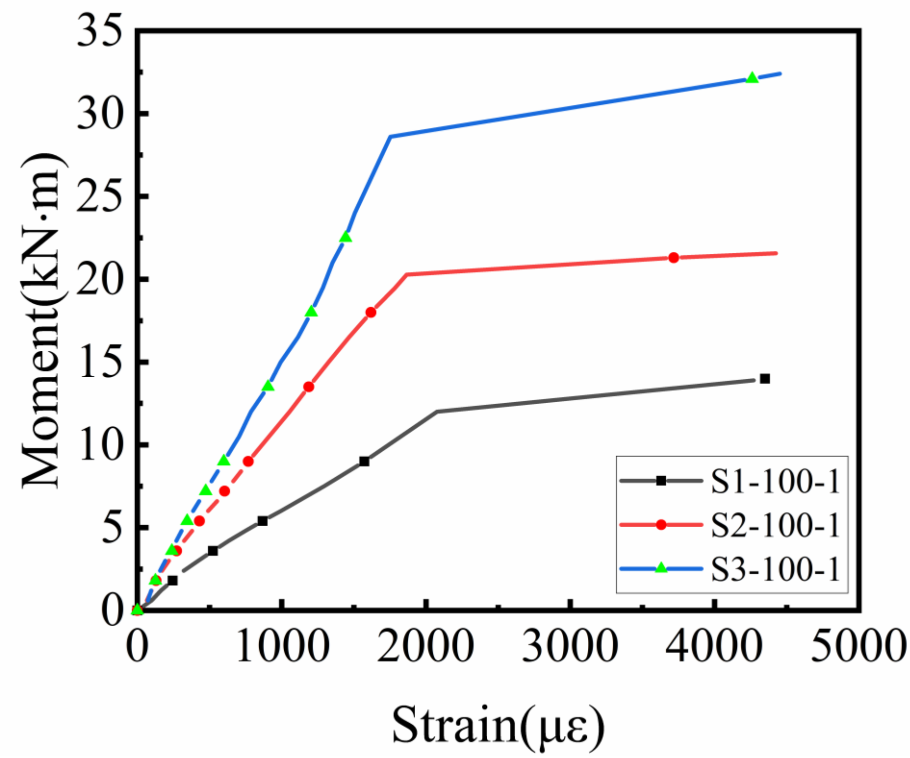

(c) Effect of rebar ratio on the moment-rebar strain relationships of the beams

Fig. 7. Moment-rebar strain relationships.

Table 5

Comparison of yield moments.

Specimens	M_y(kN.m)	$M_{y\text{-}s}$(kN.m)	M_y/M_{y-s}
N2-0-1	22.80	23.40	0.97
S1-100-1	12.74	12.00	1.06
S2-100-1	19.88	20.28	0.98
S3-100-1	27.14	28.61	0.95
S2-50-1	20.20	21.05	0.96
S2-100-0	19.50	19.20	1.02
S2-100-0.5	19.82	19.95	0.99

S2-100-1.5	20.12	20.85	0.96
N4-0-1	52.33	54.00	0.97
S4-50-1	50.44	49.08	1.03
S4-100-1	48.00	46.65	1.03

Note: M_y = the yield moment determined by the moment-curvature curve; and $M_{y\text{-}s}$ = the yield moment determined by the moment-rebar strain curve.

3.3. Crack distribution and failure mode

The distribution, width, and spacing of cracks are very important parameters when evaluating the stress state of a beam. Fig. 8 shows the distribution of cracks in the beam specimens at the end of the test. Each numeral in the figure represents the applied load (unit: kN) when the crack developed to that position. Flexural cracks were generated in the pure bending region. As the load increased, new cracks appeared continuously, and existing cracks propagated upward. After the load reached a certain level, diagonal cracks developed along the shear span. Fig. 8 shows that as the rebar ratio increased, the number of flexural cracks in the SFCGC beams increased, and the average crack spacing was smaller. Additionally, for the same rebar ratio, the average crack spacing in the SFCGC beams was smaller than that in the NC beams. This result indicates that the SFCGC beams exhibited a better bond strength between the longitudinal rebar and the concrete. However, the beam depth did not affect the crack distribution. Table 10 reports the crack width of the beams at stages 0.5 M_u, 0.6 M_u, and 0.7 M_u. These data show that as the SFVC increased, the crack width of the SFCGC beams decreased by 19%, 23%, and 13% on average at the three moments, respectively, due to the crack-arresting effect of the steel fibers.

As shown in Fig. 8, the failure mode of the SFCGC beams was similar to that of the NC beams.

After the longitudinal rebar yielded, with the further increase of load, the concrete at the top of the mid-span produced transverse cracks with a crackling sound, with the main cracks in the pure bending region developing rapidly. The crushing range of the concrete at the top of the beam is small as shown in Fig. 8. Ductile failure occurred in the beam. Thus it can be seen that the failure mode of the SFCGC beam can be judged by whether or not the rebar yields when the beam specimen is destroyed. When the failure of the beam begins with the yield of the rebar and ends with the failure of the compression zone, ductile failure occurs.

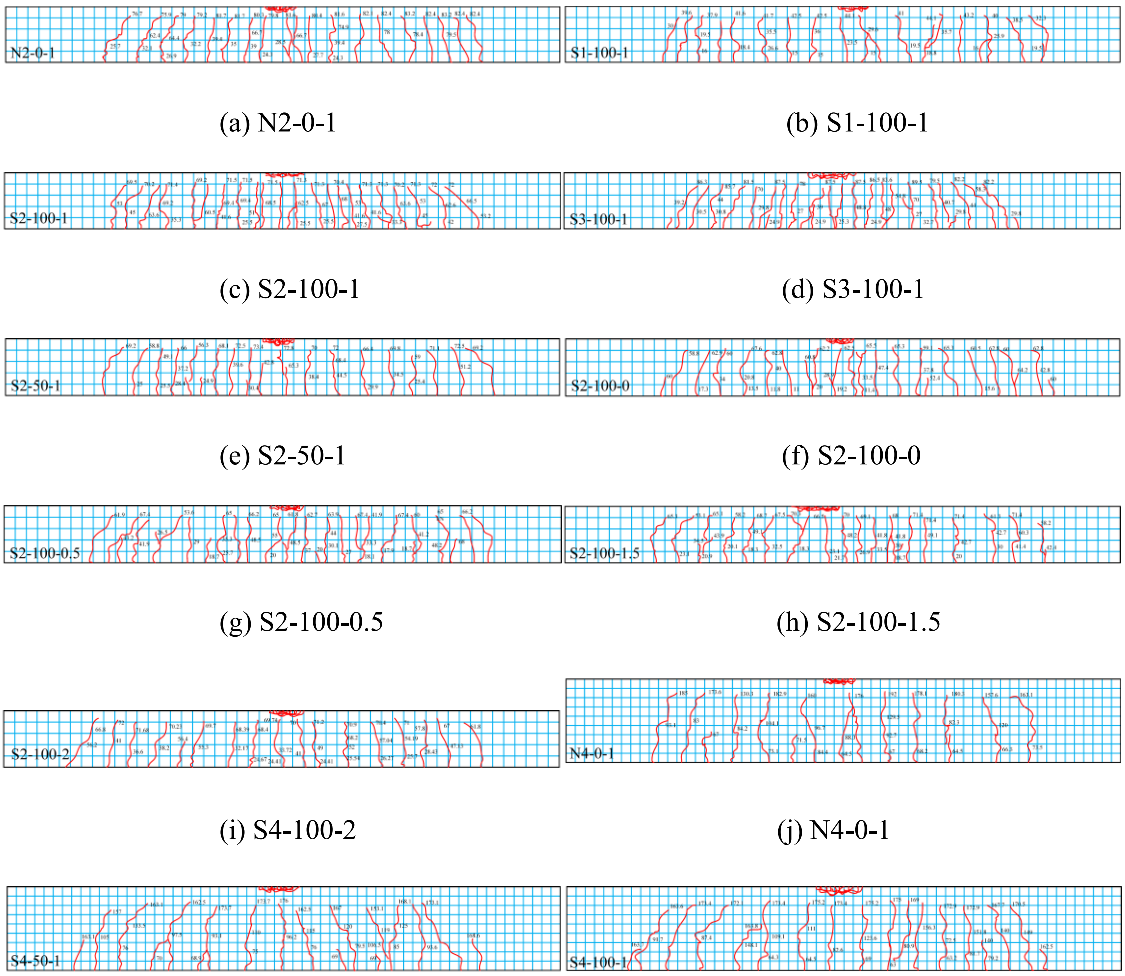

(a) N2-0-1 (b) S1-100-1

(c) S2-100-1 (d) S3-100-1

(e) S2-50-1 (f) S2-100-0

(g) S2-100-0.5 (h) S2-100-1.5

(i) S4-100-2 (j) N4-0-1

(k) S4-50-1 (l) S4-100-1

Fig. 8. Crack distribution and failure mode.

4. Theoretical analysis

4.1. Moment-curvature relationship

According to the knowledge of material mechanics, a beam subjected to vertical load has a bending curvature whose mathematical significance is equal to the second-order differential of the vertical displacement *w* with respect to *x*, while the physical significance of the curvature is the reciprocal of the radius of the bending shape (Babilio and Lenci 2017). A sketch of the beam deformation is shown in Fig. 9, where *w* is the deflection of the specimen and θ is the angle of rotation of the specimen, and the following assumptions are followed:

- Plane sections remain plane under bending so that the strain in the concrete and reinforcement is proportional to the distance from the neutral axis.
- The stresses at the centroid of each strip are assumed constant throughout its thickness.
- A perfect bond exists between the reinforcement and surrounding concrete.
- The tension strength of concrete is neglected

Let the curve be $y=f(\mathrm{x})$, as shown in Fig.10, and according to the mathematical principle, the following relationship is obtained:

$$\theta = \arctan y' \tag{1}$$

$$\frac{\mathrm{d}s}{\mathrm{d}x} = \frac{\Delta s}{\Delta x} = \sqrt{1+y'^2} \tag{2}$$

where: Δs is the curve arc length increment; and θ is the tangent line of the point and the horizontal coordinate axis of the angle increment (i.e., $\theta=\beta-\alpha$).

According to the definition of curvature (k) and the underlying mathematical theory it is known:

$$k = \left|\frac{\mathrm{d}\theta}{\mathrm{d}s}\right| = \left|\frac{\frac{\mathrm{d}\theta}{\mathrm{dx}}}{\frac{\mathrm{d}s}{\mathrm{d}x}}\right| = \left|\frac{\frac{y''}{1+y'^2}}{\sqrt{1+y'^2}}\right| = \pm\frac{y''}{\left(1+y'^2\right)^{3/2}} \tag{3}$$

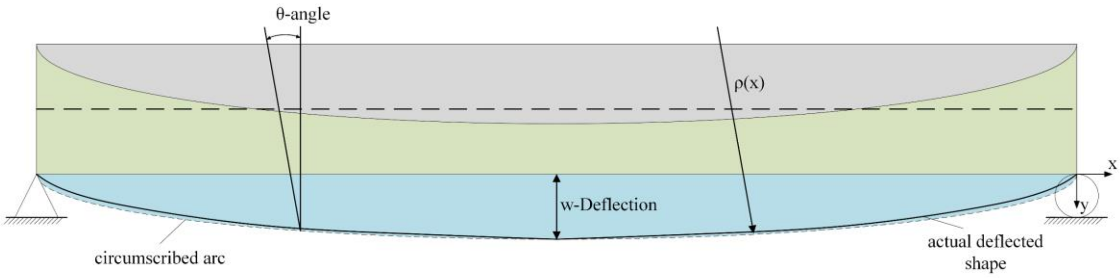

Fig. 9. Actual and assumed beam deflected shapes.

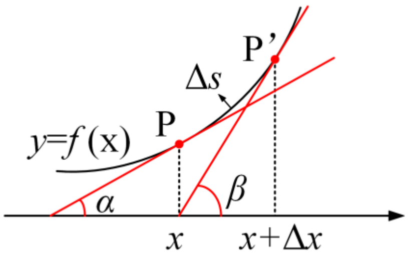

Fig. 10. Curvature calculation model.

Based on the above derivation, the curvature of the beam specimen is shown in Equation (4):

$$\phi = k = \frac{1}{\rho(x)} = \frac{\mathrm{d}^2 w}{\mathrm{d}x^2} = \pm \frac{w''}{\left(1 + w'^2\right)^{3/2}} \tag{4}$$

According to the plane section assumption, to simplify the calculation of curvature, the bending deformation curve (ACB) of the beam is approximated as a quadratic parabolic, and the calculation sketch is shown in Fig. 11. Its deformation curve equation is set as shown in Equation (5). By substituting the boundary conditions of A(0,0), C(a/2,-*f*), and B(a,0), the equation of the parabolic is obtained as shown in Equation (6), and then the quadratic derivative of the equation to obtain the final curvature calculation formula as shown in Equation (7). Due to the need for more accurate curvature measurement calculation, three measurement points are arranged in the pure bending area of the beam specimen (Fig. 4), and the bending curvature of the beam is calculated by calculating the difference between the displacement in the span and the average displacement on the left and right sides, and the formula is shown in Equation (8). This method allows the curvature of the beam to be obtained by directly measuring the displacement of the beam specimen, thus avoiding the less convenient traditional method of obtaining the curvature of the beam specimen by measuring the concrete strain and the steel strain.

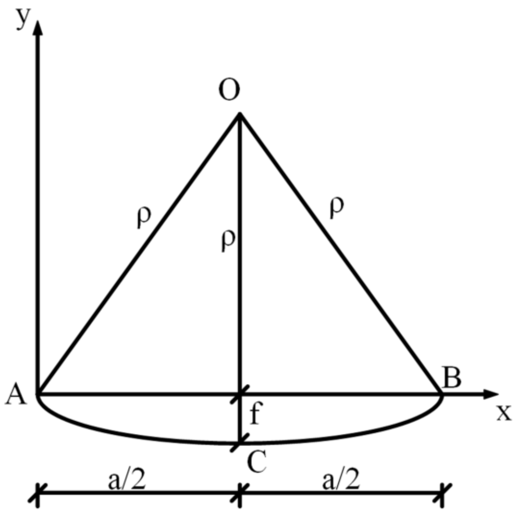

Fig. 11. Curvature of beam simplified calculation model.

$$y = c_1 x^2 + c_2 x + c_3 \tag{5}$$

$$y = \frac{4f}{a^2} x^2 - \frac{4f}{a} x \tag{6}$$

$$y'' = \frac{1}{\rho} = \frac{8f}{a^2} \tag{7}$$

$$\phi_t = \frac{8}{a^2}\left(f_3 - \frac{f_2 + f_4}{2} \right) \tag{8}$$

where c_1, c_2, c_3 are the coefficients of the quadratic parabolic equation; f_2, f_3, and f_4 are the readings of displacement gauges P2, P3, and P4 in Fig. 4, respectively; and a is the spacing of displacement gauges P2 and P4.

Table 6 shows the flexural stiffness of the specimen, which is obtained from the slope of the moment-curvature curve at each point in time. Table 7 lists the bending moments of the beam specimens at each stage. Table 8 shows the ductility coefficient (μ) (i.e., $\mu = \phi_u/\phi_y$) of each beam, which reflects the deformation capacity of the beam specimen.

Fig. 12 shows that the moment-curvature curves of the SFCGC and NC beams were almost the same. The curve of each beam from the initial stress state to the failure state can be divided into three stages. In the first stage, the moment increased linearly; then, when the moment had increased to the cracking moment, cracks appeared at the bottom of the beam, which reduced the beam's flexural stiffness. In the second stage, as the moment continued to increase, the crack width increased, and the cracks propagated upward. The curvature increased significantly after the longitudinal rebar yielded. Eventually, the beam specimen failed due to the concrete being crushed in the compression zone. The ductile failure which occurred in the specimen is in accordance with the failure law of concrete beam.

Fig. 12(a) shows the moment-curvature relationships of beams under different coal gangue replacement rates. At the same moment level, the curvature of the beams increases with the increase in the coal gangue replacement rate. The cracking moment of the beam decreases with the increase in the coal gangue replacement rate but does not change significantly (enlarged version of Fig. 12(a)).

Fig. 12(b) shows the moment-curvature relationships of beams with different steel fiber volume content. At the same moment level, the curvature of the SFCGC beams decreases with the increase in SFVC, but the magnitude is smaller. The cracking moment of the SFCGC beams increases with the increase in SFVC, and the magnitude is larger (enlarged version of Fig. 12(b)) because the steel fibers in the tensile zone after cracking can continue to bear a portion of the stress, increasing the stiffness of the cross-section after cracking.

Fig. 12(c) shows the moment-curvature relationships of the beams with different rebar ratios. At the same moment level, the curvature of the SFCGC beams decreases with increasing rebar ratio. The cracking moment of the SFCGC beams increases with increasing rebar ratio and the magnitude is larger (enlarged version of Fig. 12(c)).

Table 6

Comparison of flexural stiffness.

Specimens	B_{cr} ($\times10^{12}$N·mm^2)			$B_{s0.5}$ ($\times10^{12}$N·mm^2)			$B_{s0.6}$ ($\times10^{12}$N·mm^2)			$B_{s0.7}$ ($\times10^{12}$N·mm^2)		
	B_{exp}	B_{theo}	B_{exp}/B_{theo}	B_{exp}	B_{theo}	B_{exp}/B_{theo}	B_{exp}	B_{theo}	B_{exp}/B_{theo}	B_{exp}	B_{theo}	B_{exp}/B_{theo}
N2-0-1	3.11	2.90	1.07	1.81	1.63	1.11	1.60	1.56	1.03	1.55	1.46	1.06
S1-100-1	2.47	2.87	0.86	1.48	1.38	1.07	1.14	1.17	0.97	0.78	1.06	0.74
S2-100-1	2.69	2.87	0.94	1.50	1.61	0.93	1.38	1.52	0.91	1.22	1.46	0.84
S3-100-1	2.76	2.87	0.96	2.14	2.02	1.06	1.84	1.96	0.94	1.77	1.92	0.92
S2-50-1	2.78	2.89	0.96	1.72	1.62	1.06	1.59	1.52	1.05	1.39	1.46	0.95
S2-100-0	2.62	2.53	1.04	1.36	1.24	1.10	1.28	1.22	1.05	1.10	1.19	0.92
S2-100-0.5	2.67	2.81	0.95	1.38	1.41	0.98	1.30	1.34	0.97	1.25	1.30	0.96
S2-100-1.5	2.75	2.82	0.98	1.56	1.62	0.96	1.45	1.54	0.94	1.33	1.50	0.89
S2-100-2	2.77	2.89	0.96	1.68	1.85	0.91	1.65	1.74	0.95	1.57	1.67	0.94
N4-0-1	9.62	9.77	0.98	6.31	6.08	1.04	6.04	5.72	1.06	5.85	5.49	1.07
S4-50-1	8.57	9.74	0.88	5.83	6.07	0.96	5.46	5.71	0.96	4.76	5.48	0.87
S4-100-1	8.24	9.69	0.85	5.67	6.04	0.94	5.08	5.69	0.89	4.64	5.46	0.85

Note: B_{scr} = the initial flexural stiffness; $B_{s0.5}$, $B_{s0.6}$, and $B_{s0.7}$ = the flexural stiffness when the moment is $0.5M_u$, $0.6M_u$, and $0.7M_u$; B_{exp} = the experimental result of the flexural stiffness; and B_{theo} = the theoretical value of the flexural stiffness.

Table 7

Load-carrying capacity of beam specimens.

Specimens	M_{cr}(kN·m)			M_u(kN·m)		
	M_{exp}	M_{theo}	M_{exp}/M_{theo}	M_{exp}	M_{theo}	M_{exp}/M_{theo}
N2-0-1	7.65	8.41	0.91	25.27	23.64	1.07
S1-100-1	6.06	7.92	0.77	14.00	13.86	1.01
S2-100-1	6.59	8.63	0.76	21.57	23.54	0.92
S3-100-1	7.44	9.54	0.78	32.56	34.57	0.94
S2-50-1	7.48	8.36	0.89	22.22	23.58	0.94
S2-100-0	3.30	4.39	0.75	20.40	21.82	0.93
S2-100-0.5	5.37	6.21	0.86	20.93	22.80	0.92
S2-100-1.5	6.95	9.99	0.70	21.84	23.68	0.92
S2-100-2	7.98	11.40	0.70	21.65	24.60	0.88
N4-0-1	19.35	20.79	0.93	58.42	55.81	1.05
S4-50-1	19.23	20.68	0.93	54.21	55.66	0.97
S4-100-1	18.96	20.52	0.92	53.19	55.57	0.96

Note: M_{cr} = the cracking moment; M_u = the ultimate moment; M_{exp} = the experimental result of the moment; and M_{theo} = the theoretical value of the moment.

Table 8

Ductility of beam specimens.

Specimens	ϕ_y(10^{-5}/mm)	ϕ_u(10^{-5}/mm)	μ
N2-0-1	1.85	6.72	3.63
S1-100-1	2.23	6.45	2.89

S2-100-1	2.45	6.54	2.67
S3-100-1	2.28	5.95	2.61
S2-50-1	2.11	6.78	3.17
S2-100-0	2.78	6.31	2.26
S2-100-0.5	2.72	6.67	2.45
S2-100-1.5	2.13	6.62	3.10
S2-100-2	1.94	6.50	3.35
N4-0-1	1.37	8.84	6.45
S4-50-1	1.65	8.60	5.21
S4-100-1	1.88	8.74	4.65

Note: ϕ_y = the yield curvature; ϕ_u = the ultimate curvature; and μ = the ductility.

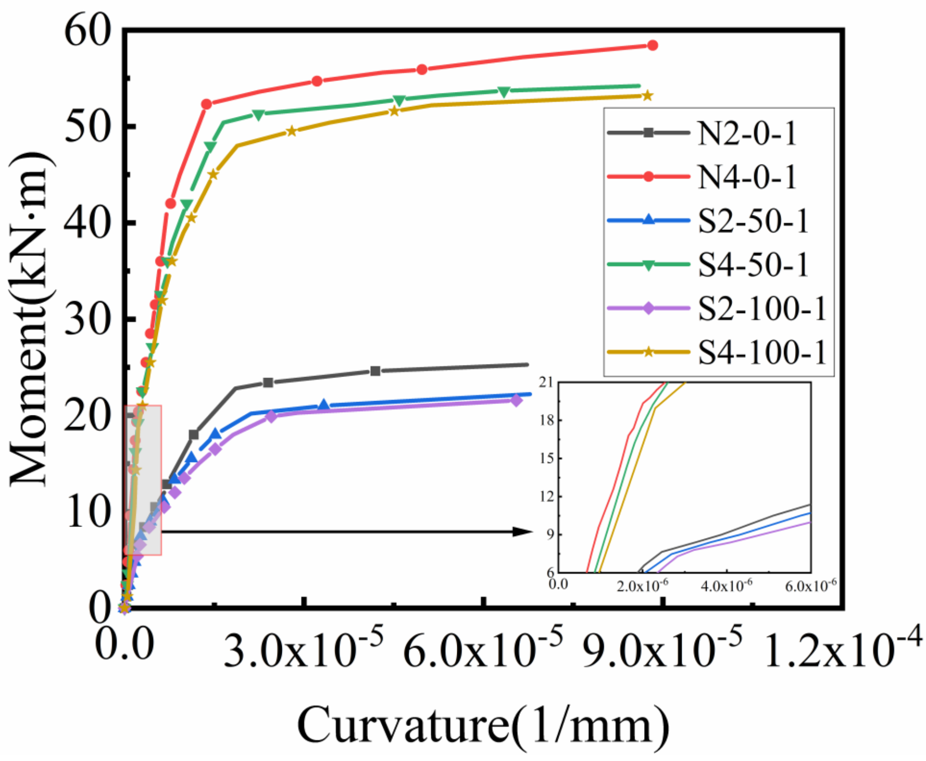

(a) Effect of coal gangue replacement rate on the moment-curvature relationships of the beams

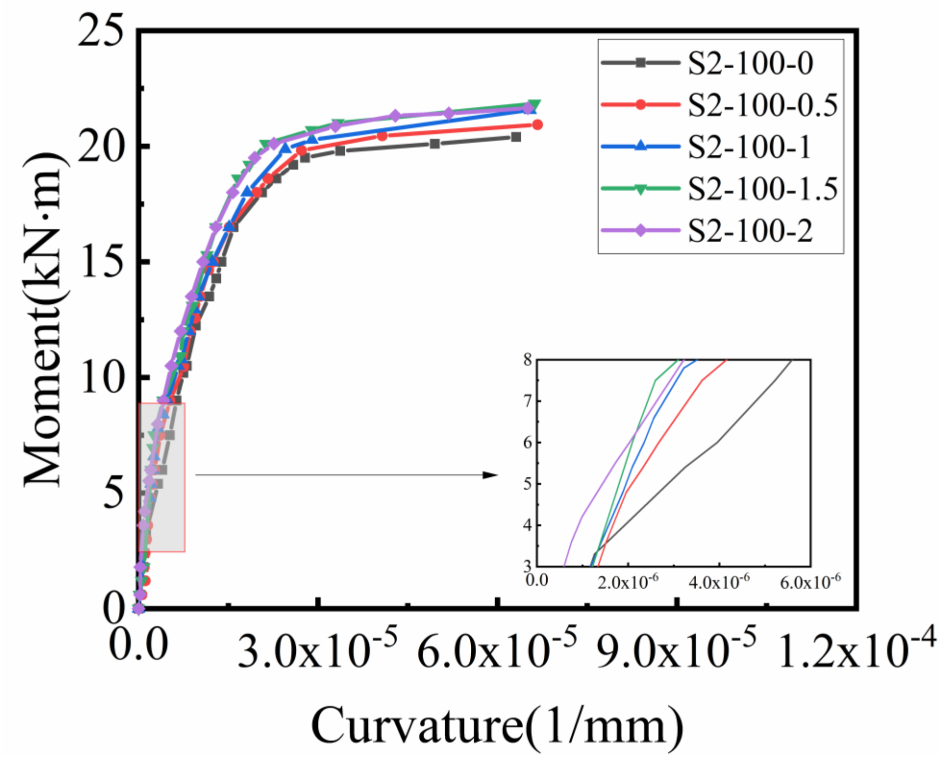

(b) Effect of SFVC on the moment-curvature relationships of the beams

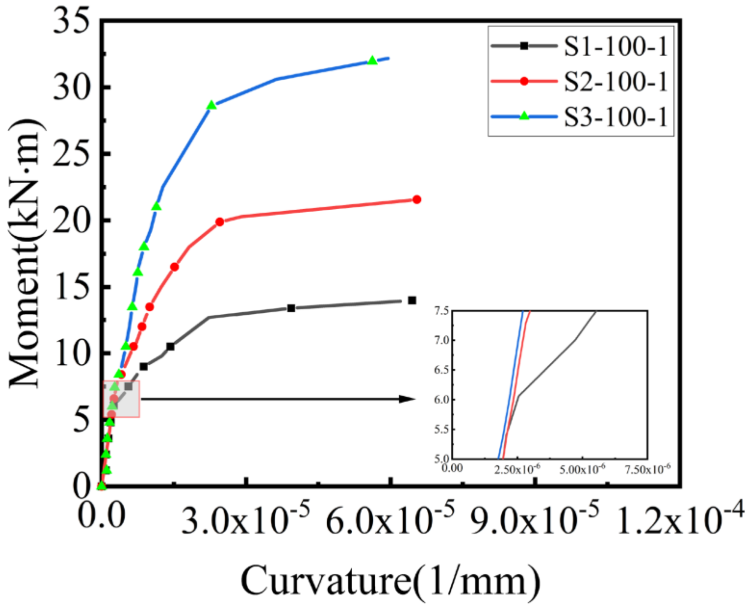

(c) Effect of rebar ratio on the moment-curvature relationships of the beams

Fig. 12. Various effects on the moment-curvature relationships of the beams.

4.2. Analysis and calculation of short-term stiffness

Considering the effect of steel fibers on structural members, CECS38:2004 (CABR 2004) and

GB 50010-2010 (CABR 2011) specify that the flexural stiffness of steel fiber-reinforced concrete members under flexure is as follows:

$$B_{fs} = B_s\left(1+\beta_B\lambda_f\right) \tag{9}$$

$$B_s = \frac{E_s A_s h_0^2}{1.15\psi + 0.2 + 6\alpha_E\rho} \tag{10}$$

$$\psi = 1.1 - 0.65\frac{f_{tk}}{\rho_{te}\sigma_s} \tag{11}$$

$$\sigma_s = \frac{M}{\eta A_s h_0} \tag{12}$$

$$\rho_{te} = \frac{A_s}{0.5bh} \tag{13}$$

where λ_f is the characteristic value of the steel fiber content (i.e., $\lambda_f = \rho_f l_f/d_f$); ρ_f is the SFVC, l_f is the length of the steel fiber; d_f is the diameter of the steel fiber; β_B is the influence coefficient of the steel fiber on the short-term stiffness of the steel fiber-reinforced concrete member under flexure, generally set to 0.35; f_y is the yield strength of the rebar; A_s is the cross-sectional area of the longitudinal rebar; E_s is the elastic modulus of the rebar; α_E is the ratio of the elastic modulus of the rebar to the elastic modulus of the concrete; ψ is the coefficient related to the strain heterogeneity of the longitudinal rebar between cracks; σ_s is the stress in the longitudinal rebar, calculated from $M = 0.5M_u$, $0.6M_u$, and $0.7M_u$ and the corresponding coefficient η (i.e., η = 0.87); f_{tk} is the tensile strength of the concrete; and ρ_{te} is the longitudinal rebar ratio calculated from the cross-sectional area of the effective tensile concrete.

The initial flexural stiffness is evaluated using B_{scr}=0.85E_cI_0, where E_c is the elastic modulus of the concrete and I_0 is the moment of inertia of the transformed section. According to GB50010-2010 (CABR 2011), the flexural stiffness under service conditions is estimated using bending moments of 0.5 M_u, 0.6 M_u, and 0.7 M_u. Table 6 compares the predicted and experimental results of each flexural stiffness. The ratio of the experimental results to the predicted value is in the range of 0.74-1.11 and the correlation coefficient R^2 is 0.991069, indicating that the predicted results are in good agreement with the experimental results. Therefore, the current design code is applicable for predicting the short-term stiffness of the SFCGC beams under flexure.

4.3. Analysis and calculation of crack width

4.3.1. Calculation of average crack spacing

To the best of our knowledge, a calculation of the average crack spacing of the SFCGC beams has not been reported. The experimental results showed that the number and width of cracks in the SFCGC beams differed from those in the NC beams, mainly due to the low elastic modulus of the lightweight aggregate concrete, which is approximately 25% less than that of conventional concrete of the same grade. In this study, the average crack spacing were calculated using the methods in CECS38:2004 (CABR 2004) and GB 50010-2010 (CABR 2011), as specifically shown in Equation (14). The correlation coefficient in the equation is adjusted by regression fitting of the experimental results.

$$l_{\mathrm{m}} = k_1 C_{\mathrm{s}} + k_2 \frac{d_{\mathrm{eq}}}{\rho_{\mathrm{te}}\left(1+\alpha_{\mathrm{t}}\lambda_{\mathrm{f}}\right)} \tag{14}$$

$$d_{\mathrm{eq}} = \frac{\sum n_{\mathrm{i}} d_{\mathrm{i}}^2}{\sum n_{\mathrm{i}} v_{\mathrm{i}} d_{\mathrm{i}}} \tag{15}$$

where α_{t} is the coefficient of influence of the steel fiber on the tensile strength of the steel fiber-reinforced concrete, which is generally taken as 0.26; d_{eq} is the equivalent diameter of the tensile rebar; C_{s} is the thickness of the concrete cover of the tensile rebar; d_{i} is the nominal diameter of the i-th longitudinal rebar in the tension zone; n_{i} is the number of longitudinal rebar members in the tension zone; and v_{i} is the relative bond characteristic coefficient of the i-th longitudinal rebar in the tension zone, which is generally taken as 1.0.

Through a regression analysis of the experimental results of 12 beams, a fitting curve with d_{eq}/ρ_{te} as the independent variable and l_m as the dependent variable is obtained, as shown in Fig. 13. The average crack spacing is calculated using Equation (16):

$$l_m = 2.5C_s + 0.03\frac{d_{eq}}{\rho_{te}\left(1+\alpha_t\lambda_f\right)} \tag{16}$$

The experimental results and the values calculated by Equation (16) are shown in Table 9. The ratio of the experimental results to the predicted value is in the range of 0.98-1.05 and the correlation coefficient R^2 is 0.999087, indicating that the predicted results are in good agreement with the experimental results.

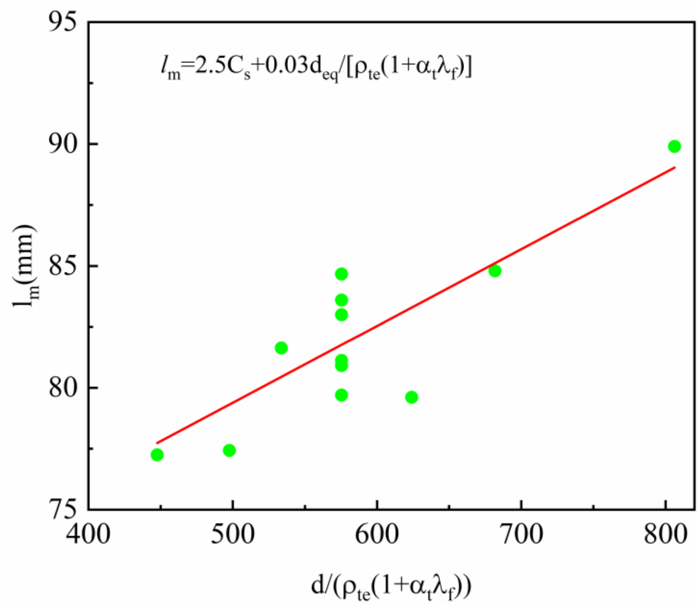

Fig. 13. Fitted curve of average crack spacing.

Table 9

Calculated and experimental results of average cracking spacing.

Specimens	$l_{m,exp}$/mm	$l_{m,theo}$/mm	$l_{m,exp}/l_{m,theo}$
N2-0-1	83.60	79.76	1.05
S1-100-1	89.92	86.68	1.04

S2-100-1	79.71	79.76	1.00
S3-100-1	77.25	75.93	1.02
S2-50-1	80.91	79.76	1.01
S2-100-0	84.80	82.95	1.02
S2-100-0.5	79.61	81.22	0.98
S2-100-1.5	81.63	78.51	1.04
S2-100-2	78.82	77.43	1.02
N4-0-1	81.12	79.76	1.02
S4-50-1	82.67	79.76	1.04
S4-100-1	83.00	79.76	1.04

Note: $l_{\mathrm{m,exp}}$ = the experimental result of the cracking spacing; and $l_{\mathrm{m,theo}}$ = the theoretical value of the cracking spacing.

4.3.2. Calculation of crack width

According to CECS38:2004 (CABR 2004) and GB 50010-2010 (CABR 2011) and the optimized equation for calculating the crack spacing, the average crack width (w_{fm}) can be calculated by Equation (17):

$$w_{\mathrm{fm}} = \left(1 - \beta_{\mathrm{cw}} \lambda_{\mathrm{f}}\right) \alpha_{\mathrm{c}} \psi \frac{\sigma_{\mathrm{s}}}{E_{\mathrm{s}}} l_{\mathrm{m}} \tag{17}$$

where α_{c} is the coefficient of influence of the tensile deformation of concrete, which is taken as 0.77 according to GB 50010-2010 (CABR 2011); β_{cw} is the coefficient of influence of the steel fibers on the cracks in the steel fiber-reinforced concrete members, which is generally taken as 0.35; and ψ is calculated by Equation (11), and σ_{s} is calculated using Equation (12).

The experimental results and the values calculated by Equation (17) are shown in Table 10. The ratio of the experimental results to the predicted value is in the range of 0.93-1.05 and the correlation coefficient R^2 is 0.998921, indicating that the predicted results are in good agreement with the test results.

Table 10

Calculated and experimental results of the average crack width.

Specimens	$0.5M_u$			$0.6M_u$			$0.7M_u$		
	w_{exp}	w_{theo}	w_{exp}/w_{theo}	w_{exp}	w_{theo}	w_{exp}/w_{theo}	w_{exp}	w_{theo}	w_{exp}/w_{theo}
N2-0-1	0.044	0.042	1.05	0.059	0.056	1.05	0.068	0.070	0.97
S1-100-1	0.029	0.028	1.04	0.048	0.046	1.04	0.064	0.063	1.02
S2-100-1	0.041	0.042	0.98	0.055	0.056	0.98	0.072	0.070	1.03
S3-100-1	0.042	0.043	0.98	0.057	0.055	1.04	0.068	0.067	1.01
S2-50-1	0.041	0.042	0.98	0.058	0.056	1.04	0.067	0.070	0.96
S2-100-0	0.053	0.055	0.96	0.074	0.071	1.04	0.085	0.087	0.98
S2-100-0.5	0.049	0.050	0.98	0.063	0.066	0.95	0.083	0.081	1.02
S2-100-1.5	0.039	0.041	0.95	0.053	0.054	0.98	0.067	0.066	1.02
S2-100-2	0.032	0.034	0.94	0.044	0.045	0.97	0.059	0.056	1.05
N4-0-1	0.043	0.042	1.02	0.052	0.056	0.93	0.068	0.070	0.97
S4-50-1	0.044	0.042	1.05	0.054	0.056	0.96	0.069	0.070	0.99
S4-100-1	0.041	0.042	0.98	0.058	0.056	1.04	0.071	0.070	1.01

Note: w_{exp} = the experimental result of the average crack width; and w_{theo} = the theoretical value of the average crack width.

4.4. Analysis and calculation of bearing capacity

4.4.1. Calculation of cracking moment

The cracking moment (M_{cr}) of each beam can be obtained according to the cracking load from the test and can also be theoretically calculated by, for example, Equation (18) (Guo and Shi 2003; CABR 2004).

$$M_{\mathrm{cr}} = \gamma f_{\mathrm{ft}} W_0 \tag{18}$$

$$\gamma = \left(0.7 + \frac{120}{h}\right)\gamma_{\mathrm{m}} \tag{19}$$

$$W_0 = \frac{I_0}{h - x_0} \tag{20}$$

$$I_0 = \frac{b}{3}\left[x_0^3 + \left(h - x_0\right)^3\right] + \left(n-1\right)A_{\mathrm{s}}\left(h_0 - x_0\right)^2 \tag{21}$$

$$x_0 = \left[\frac{1}{2}bh^3 + \left(n-1\right)A_{\mathrm{s}}h_0\right] / A_0 \tag{22}$$

$$f_{\mathrm{ft}} = f_{\mathrm{tk}}\left(1 + \alpha_{\mathrm{t}}\lambda_{\mathrm{f}}\right) \tag{23}$$

where f_{ft} is steel fiber-reinforced concrete axial tensile strength; γ is the plastic influence coefficient of the section under flexure; γ_{m} is the basic value of the plastic influence coefficient of the section under flexure, which is taken as 1.55 according to GB 50010-2010 (CABR 2011); W_0 is the moment of resistance of the section; I_0 is the moment of inertia of the transformed section; A_0 is the transformed cross-sectional area, $A_0 = A_{\mathrm{c}} + (n-1) A_{\mathrm{s}}$; A_{c} is the cross-sectional area of the ordinary concrete in the specimen; n is the ratio of the elastic modulus of the rebar to the elastic modulus of the concrete; and x_0 is the depth of the concrete compression zone.

The experimental results and the values calculated by Equation (18) are shown in Table 7. The ratio of the experimental results to the predicted value is in the range of 0.70-0.93 and the correlation coefficient R^2 is 0.982778, indicating that the predicted results are in good agreement with the experimental results.

4.4.2. Calculation of ultimate moment

According to CECS38:2004 (CABR 2004), the ultimate moment (M_u) of the SFCGC beam is calculated by Equation (24), and the calculation diagram is shown in Fig. 14:

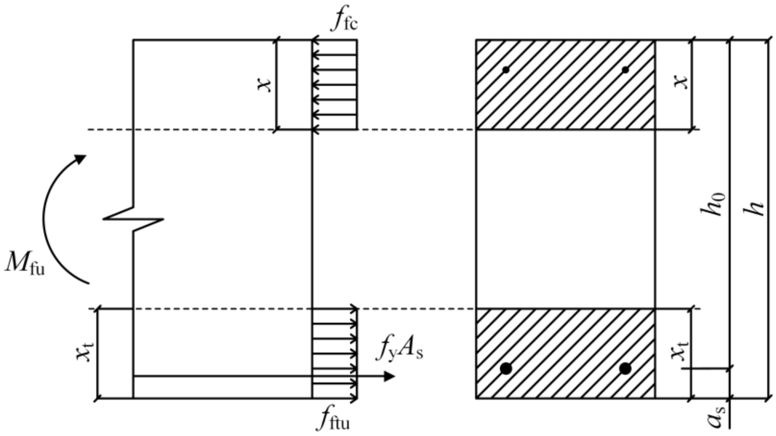

Fig. 14. Calculation diagram of the flexural bearing capacity of the beams.

$$M_{fu} = f_{fc}bx\left(h_0 - \frac{x}{2}\right) - f_{ftu}bx_t\left(\frac{x_t}{2} - a\right) \tag{24}$$

$$x = \frac{f_y A_s + f_{ftu}bx_t}{f_{fc}b} \tag{25}$$

$$f_{ftu} = f_t \beta_{tu} \lambda_f \tag{26}$$

where f_{fc} is the axial compressive strength of the steel fiber-reinforced concrete; f_{ftu} is the tensile strength of the equivalent rectangular stress block of the steel fiber-reinforced concrete in the tension zone; β_{tu} is the coefficient of influence of steel fibers on the tensile effect of the steel fiber concrete in the tension zone in a normal section of the steel fiber-reinforced concrete member, which is taken as 1.30 according to the specification; x is the depth of the concrete compression zone, which is assumed to be an equivalent rectangular block; x_t is the depth of the equivalent rectangular stress block in the tension zone, where $x_t = h - x/\beta_1$ with the coefficient β_1 taken as 0.8 for concrete with a strength grade not exceeding C50 according to GB 50010-2010 (CABR 2011); and a is the distance from the resultant point of the longitudinal tensile rebar to the edge of the tension zone of the main section.

The experimental results and the values calculated by Equation (24) are shown in Table 7. The ratio of the experimental results to the predicted value is in the range of 0.92-1.07 and the correlation coefficient R^2 is 0.997418, indicating that the predicted results are in good agreement with the experimental results.

5. Parametric Analysis

5.1. Effect of beam depth

Fig. 12(a) compares the moment-curvature relationships of beams with different beam depths for the same SFVC (1%) and rebar ratio (almost 1.1%) for each coal gangue replacement rate. As the beam height increases from 200 mm to 300 mm, the load-carrying capacity and flexural stiffness of both the SFCGC and NC beams increase.

5.2. Effect of coal gangue replacement rate

Fig. 15 exhibits the effects of the coal gangue replacement rate on the flexural stiffness, bending moment, and ductility of the beam specimens with an SFVC of 1% and a rebar ratio of 1.17%. Fig. 15 and Tables 6-8 show that with an increase in the coal gangue replacement rate, on average, the initial flexural stiffness and the effective flexural stiffness of the beams decreased by 12% and 11%, respectively, the cracking moment and the ultimate moment decreased by 8% and 13%, respectively, and the ductility decreased by 20%. The coal gangue replacement rate had little effect on the cracking moment and the effective flexural stiffness of the beams but had a significant effect on the initial flexural stiffness because the elastic modulus of the SFCGC was lower than that of the NC.

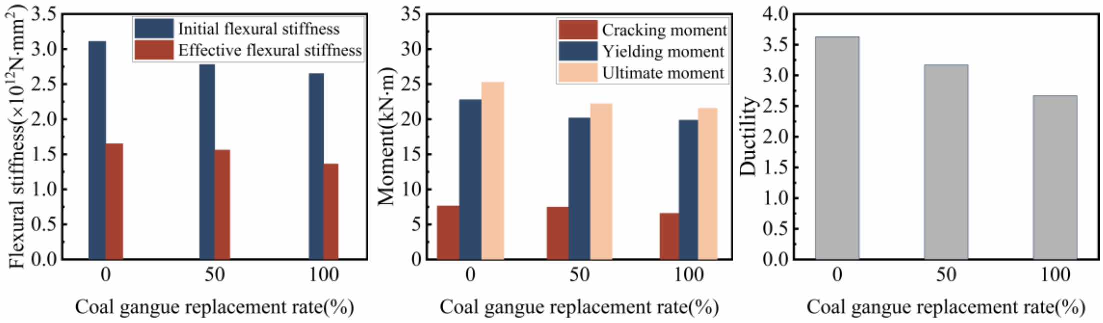

(a) Flexural stiffness (b) Moment (c) Ductility

Fig. 15. Effect of coal gangue replacement rate on the flexural behavior of beams.

5.3. Effect of steel fiber volume content

Fig. 16 exhibits the effects of SFVC on the flexural stiffness, bending moment, and ductility of the beam specimens with a coal gangue replacement rate of 100% and a rebar ratio of 1.17%. As seen from Fig. 16 and Tables 6-8, the cracking moment of the SFCGC beams increased by 91% on average compared with that of the beam without steel fibers. This result occurred due to the crack-arresting effect of the steel fibers. The incorporation of steel fibers caused the tensile strength of the SFCGC beams to increase by an average of 39.24% higher on average (Table 3). When the SFVC exceeded 1%, the tensile strength and cracking moment of the SFCGC beams increased nonsignificantly. Hence, the SFVC should not be greater than 1% from the perspective of the optimal utilization of steel fibers. In addition, the SFVC had little effect on the ultimate moment and the initial flexural stiffness of the SFCGC beams, which increased by 5.3% and 3.8% on average, respectively, whereas the effective flexural stiffness and ductility of the SFCGC beams increased by 15.7% and 27.9% on average, respectively, with an increase in the SFVC.

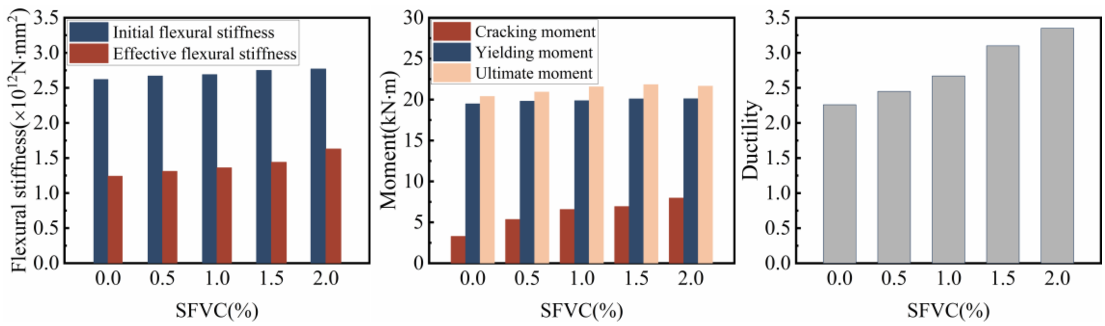

(a) Flexural stiffness (b) Moment (c) Ductility

Fig. 16. Effect of SFVC on the flexural behavior of the beams.

5.4. Effect of rebar ratio

Fig. 17 compares the effect of the rebar ratio on the flexural stiffness, bending moment, and ductility of the beam specimens when the coal gangue replacement rate is 100% and the SFVC is 1%. Fig. 17 shows that the yielding moment and ultimate bending moment of the SFCGC beams increase significantly with the increase in rebar ratio, while the ductility decreases significantly. The rebar ratio has a minimal effect on the initial flexural stiffness, but the effective flexural stiffness is improved by increasing the rebar ratio. With the increase of rebar ratio, the effective flexural stiffness of the SFCGC beams increases by 39.66% on average. The reason is that in the cracking stage of the beam, the initial stiffness of the beam is mainly affected by the elastic modulus of concrete. After the beam cracks, the beam enters the stage of cooperative work between rebar and concrete, so the flexural stiffness of the beam is affected by the performance of the rebar. High rebar ratio is an effective method to improve the bearing capacity and bending stiffness of the SFCGC beams whose strength is lower than that of NC beams.

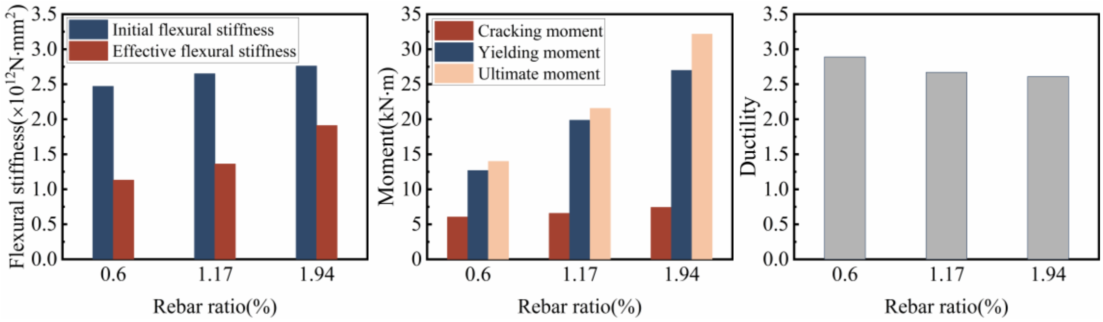

(a) Flexural stiffness (b) Moment (c) Ductility

Fig. 17. Effect of rebar ratio on the flexural behavior of the beams.

6. Conclusions

In this study, a simple calculation formula for curvature measurement is proposed, and the current design code formulas for flexural stiffness, crack calculation, cracking moment, and ultimate moment of the SFCGC beams are optimized. And the calculation results are compared with the experimental results. The main conclusions are as follows:

1. In this study, the moment-curvature calculation method is simplified by the knowledge of material mechanics and mathematical theory. The curvature of SFCGC beams can be obtained by measuring the displacement of the SFCGC beams and calculating it, avoiding the need to obtain the curvature of the specimen by measuring concrete strain and steel strain, which greatly reduces the test workload and improves the test efficiency.

2. With the increment of coal gangue replacement rate, the load-carrying capacity of the SFCGC beams decreases compared with the NC beams, but the cracking moment of the SFCGC beams can be improved by incorporating steel fibers, and the ultimate moment of the SFCGC beams by increasing the rebar ratio. The flexural stiffness and ductility of the SFCGC beams increased with the increment of steel fiber volume content. With the increment of rebar ratio, the ultimate moment and flexural stiffness of the SFCGC beams increase substantially but the ductility decreases.

3. Based on regression analysis of the experimental results, the equations for calculating the average crack spacing and average crack width of the SFCGC beams were proposed. The calculated results are in good agreement with the experimental results, thereby providing a simple and feasible method for calculating the average crack spacing and average crack width of the SFCGC beams.

4. The design methods in current codes predict the SFCGC beams experimental results well in terms of cracking moments, ultimate moments, and flexural stiffness. The mean value of the $M_{cr,exp}/M_{cr,theo}$, $M_{u,exp}/M_{u,theo}$, and B_{exp}/B_{theo} ratio was 0.77, 0.97, and 0.97, respectively. The error between the experimental value and the calculated value was small. This provides a reference for the subsequent theoretical research and practical engineering application of coal gangue concrete components.

Acknowledgments

This research was financially supported by the Foundation of China Scholarship Council (No. 201805975002), Jilin Provincial Science and Technology Development Plan Project of China (No. 20220203082SF), a scientific research projects from the Education Department of Jilin Province of China (No. JJKH20210279KJ). Guangxi Natrual Science foundation (2021JJA160189), National Natural Science Foundation of China (No. 51968013). Guangxi Natural Science Foundation of (No. 2021JJA160189). The authors wish to acknowledge the sponsors. However, any opinions, findings, conclusions and recommendations presented in this paper are those of the authors and do not necessarily reflect the views of the sponsors.

Reference

Atiş, C. D., & Karahan, O. (2009). Properties of steel fiber reinforced fly ash concrete. *Construction and Building Materials*, *23*(1), 392-399, http://doi.org/10.1016/j.conbuildmat.2007.11.002.

Babilio, E., & Lenci, S. (2017). On the notion of curvature and its mechanical meaning in a geometrically exact plane beam theory. International Journal of Mechanical Sciences, 128, 277-293.

Brandt, A. M. (2008). Fibre reinforced cement-based (FRC) composites after over 40 years of development in building and civil engineering. *Composite structures*, *86*(1-3), 3-9, http://doi.org/10.1016/j.compstruct.2008.03.006.

CABR (China Academy of Building Research). 2003. Standard for test method of performance on ordinary fresh concrete. (GB/T 50080-2002). China: CABR.

CABR (China Academy of Building Research). 2004. Technical specification for fiber reinforced concrete structures (CECS38:2004). China: CABR.

CABR (China Academy of Building Research). 2011. Code for design of concrete structures (GB 50010-2010). China: CABR.

CABR (China Academy of Building Research). 2012. Standard for test methods of concrete structures. (GB/T 50152-2012). China: CABR.

CABR (China Academy of Building Research). 2019. Standard for test methods of concrete physical and mechanical properties (GB/T 50081-2019). China: CABR.

Cai, B., Li, K., & Fu, F. (2023, June). Flexural behavior of steel fiber-reinforced coal gangue aggregate concrete beams. In Structures (Vol. 52, pp. 131-145). Elsevier.

https://doi.org/10.1016/j.istruc.2023.03.172.

Chen, X., Wan, D. W., Jin, L. Z., Qian, K., & Fu, F. (2019). Experimental studies and microstructure analysis for ultra high-performance reactive powder concrete. Construction and Building Materials, 229, 116924, https://doi.org/10.1016/j.conbuildmat.2019.116924.

Du, Y., Wang, J., Shi, C., Hwang, H. J., & Li, N. (2021). Flexural behavior of alkali-activated slag-based concrete beams. Engineering Structures, 229, 111644.

Foroughi, S., & Yüksel, S. B. (2020). Investigation of the moment–curvature relationship for reinforced concrete square columns. Turkish Journal of Engineering, 4(1), 36-46.

Fu, F., Lam, D., Ye, J.(2010), Moment resistance and rotation capacity of semi-rigid composite connections with precast hollowcore slabs,Journal of Constructional Steel Research, 2010, 66(3), pp. 452–461

Fu, F., Parke, G.A.R.(2018), Assessment of the Progressive Collapse Resistance of Double-Layer Grid Space Structures Using Implicit and Explicit Methods ,International Journal of Steel Structures, 2018, 18(3), pp. 831–842

Gao, S., Guo, L., Fu, F., Zhang, S.(2017)Capacity of semi-rigid composite joints in accommodating column loss,Journal of Constructional Steel Research, 2017, 139, pp. 288–301

Gao, S., Zhao, G. H., Guo, L. H., Zhou, L. Q., & Yuan, K. K. (2021). Utilization of coal gangue as coarse aggregates in structural concrete. *Construction and Building Materials*, *268*, 121212, https://doi.org/10.1016/j.conbuildmat.2020.121212.

Gong, C., Yan, J., Liu, J., & Yu, H. (2016). Biology Migration and Distribution Characteristics of Trace Elements in Reconstructed Soil with Coal Gangue Filling. *Agricultural Science & Technology, 17(9)*, 2167.

Guo, J. M., & Zhu, L. L. (2011). Experimental research on durabilities of coal gangue concrete. In Advanced Materials Research (Vol. 306, pp. 1569-1575). Trans Tech Publications Ltd, https://doi.org/10.4028/www.scientific.net/AMR.306-307.1569.

Guo, Y., Yan, K., Cui, L., & Cheng, F. (2016). Improved extraction of alumina from coal gangue by surface mechanically grinding modification. *Powder Technology*, *302*, 33-41, http://dx.doi.org/10.1016/j.powtec.2016.08.034.

Guo, Z. H., & Shi, X. D. (2003) Reinforced concrete theory and analyse. *Tsinghua University Press*. (in Chinese)

Hadhood, A., Mohamed, H. M., & Benmokrane, B. (2018). Flexural stiffness of GFRP-and CFRP-RC circular members under eccentric loads based on experimental and curvature analysis. ACI Struct. J, 115(4), 1185-1198.

Hasan, H. A., Karim, H., Sheikh, M. N., & Hadi, M. N. (2019). Moment-curvature behavior of glass fiber-reinforced polymer bar-reinforced normal-strength concrete and high-strength concrete columns. ACI Structural Journal, 116(4), 65-75.

Jabłońska, B., Kityk, A. V., Busch, M., & Huber, P. (2017). The structural and surface properties of natural and modified coal gangue. *Journal of environmental management, 190*, 80-90, https://doi.org/10.1016/j.jenvman.2016.12.055.

Jia, J., Cao, Q., Zhang, L., & Zhou, J. (2021). Flexural performance of reinforced concrete beams made by innovative post-filling coarse aggregate process. Advances in Structural Engineering, 24(13), 2898-2911.

Jin-min, G. (2011, May). Experimental research on performances of concrete with coal gangue. *In 2011 International Conference on Materials for Renewable Energy & Enviro* *nment (Vol. 2, pp. 1988-1991)*. IEEE, 10.1109/ICMREE.2011.5930728.

Karimaei, M., Dabbaghi, F., Sadeghi-Nik, A., & Dehestani, M. (2020). Mechanical performance of green concrete produced with untreated coal waste aggregates. *Construction and Building Materials*, *233*, 117264, https://doi.org/10.1016/j.conbuildmat.2019.117264.

Katzer, J., & Domski, J. (2012). Quality and mechanical properties of engineered steel fibres used as reinforcement for concrete. *Construction and Building Materials*, *34*, 243-248, http://dx.doi.org/10.1016/j.conbuildmat.2012.02.058.

Kwak, H. G., & Kim, S. P. (2002). Nonlinear analysis of RC beams based on moment–curvature relation. Computers & structures, 80(7-8), 615-628.

Li, D., Song, X., Gong, C., & Pan, Z. (2006). Research on cementitious behavior and mech anism of pozzolanic cement with coal gangue. *Cement and Concrete Research, 36 (9)*, 1752-1759, https://doi.org/10.1016/j.cemconres.2004.11.004.

Li, Y., Yao, Y., Liu, X. M., Sun, H. H., & Ni, W. (2013). Improvement on pozzolanic reactivity of coal gangue by integrated thermal and chemical activation. *Fuel*, *109*, 527-533, http://dx.doi.org/10.1016/j.fuel.2013.03.010.

Liu, H. Q., Xu, Q., Wang, Q. H., & Zhang, Y. Z. (2020). Prediction of the elastic modulus of concrete with spontaneous-combustion and rock coal gangue aggregates, *Structures, 28*, 774-785, https://doi.org/10.1016/j.istruc.2020.09.021.

Ma, H. Q., Yi, C., Zhu, H. G., Dong, Z. C., Chen, H. Y., Wang, J. X., & Li, D. Y. (2018). Compressive strength and durability of coal gangue aggregate concrete. *Mater. Rep. B*, *32*, 2390-2395, http://doi.org/10.11896/j.issn.1005-023X.2018.14.012.

Ma, H. Q., Zhu, H. G., Wu, C., Chen, H. Y., Sun, J. W., & Liu, J. Y. (2020). Study on compressive strength and durability of alkali-activated coal gangue-slag concrete and its mechanism. *Powder Technology*, *368*, 112-124, https://doi.org/10.1016/j.powtec.2020.04.054.

Moghadam, M. J., Ajalloeian, R., & Hajiannia, A. (2019). Preparation and application of alkali-activated materials based on waste glass and coal gangue: A review. *Construction and Building Materials*, *221*, 84-98, https://doi.org/10.1016/j.conbuildmat.2019.06.071.

Mohammadi, Y., Singh, S. P., & Kaushik, S. K. (2008). Properties of steel fibrous concrete containing mixed fibres in fresh and hardened state. *Construction and Building Materials*, *22*(5), 956-965, https://doi.org/10.1016/j.conbuildmat.2006.12.004.

Olivito, R. S., & Zuccarello, F. A. (2010). An experimental study on the tensile strength of steel fiber reinforced concrete. *Composites Part B: Engineering*, *41*(3), 246-255, https://doi.org/10.1016/j.compositesb.2009.12.003.

Priestley, M. J. N., Park, R., & Lu, F. P. S. (1971). Moment-curvature relationships for prestressed concrete in constant-moment zones. Magazine of Concrete Research, 23(75-76), 69-78.

Qian K, Geng SY, Liang SL, Fu F, Yu J,(2022) Effects of loading regimes on the structural behavior of RC beam-column sub-assemblages against disproportionate collapse, Engineering Structures 251, 113470

Qian K, Lan,DQ, Fu, F, Li B (2020), Effects of infilled wall opening on load resisting capacity of RC frames to mitigate progressive collapse risk, Engineering Structures 223, 111196

Qian K, Liang SL, Feng DC, Fu F, Wu G （2020）, Experimental and numerical investigation on progressive collapse resistance of post-tensioned precast concrete beam-column sub-assemblages，*Journal of Structural Engineering 146* (9)

Qian K, Weng YH ,Fu,, F, Deng XF （2021）， Numerical evaluation of the reliability of using single-story substructures to study progressive collapse behaviour of multi-story RC frames， *Journal of Building Engineering 33*, 101636

Qin, J. G., Zhao, R. D., Chen, T. J., Zi, Z. Y., & Wu, J. H. (2019). Co-combustion of municipal solid waste and coal gangue in a circulating fluidized bed combustor. *International Journal of Coal Science & Technology*, *6*(2), 218-224, http://doi.org/10.1007/s40789-018-0231-4.

Qin, L., & Gao, X. (2019). Properties of coal gangue-Portland cement mixture with carbonat ion. Fuel, 245, 1-12, https://doi.org/10.1016/j.fuel.2019.02.067.

Schreier, H., Orteu, J. J., & Sutton, M. A. (2009). *Image correlation for shape, motion and deformation measurements: Basic concepts, theory and applications* (Vol. 1). Boston, MA: Springer-Verlag US, https://doi.org/10.1007/978-0-387-78747-3.

Sun, Y. X., & Li, X. D. (2011). Development and design of coal gangue concrete filling material. In *Advanced Materials Research* (Vol. 295, pp. 1198-1201). Trans Tech Publications Ltd, https://doi.org/10.4028/www.scientific.net/AMR.295-297.1198.

Viet, N. V., & Zaki, W. (2019). Analytical investigation of the behavior of concrete beams reinforced with multiple circular superelastic shape memory alloy bars. Composite Structures, 210, 958-970.

Wang, L., Shen, N., Zhang, M., Fu, F., & Qian, K. (2020). Bond performance of Steel-CFRP bar reinforced coral concrete beams. *Construction and Building Materials*, *245*, 118456.

Wang, Z., & Zhao, N. (2015). Influence of coal gangue aggregate grading on strength properties of concrete. *Wuhan University Journal of Natural Sciences*, 20(1), 66-72, https://doi.org/10.1007/s11859-015-1060-6.

Wu, J., Bai, G. L., Wang, P., & Liu, Y. (2018). Mechanical properties of a new type of block made from shale and coal gangue. *Construction and Building Materials*, *190*, 796-804, https://doi.org/10.1016/j.conbuildmat.2018.09.130.

Wu, T., Sun, Y., Liu, X., & Cao, Y. (2021). Comparative study of the flexural behavior of steel fiber-reinforced lightweight aggregate concrete beams reinforced and prestressed with CFRP tendons. Engineering Structures, 233, 111901.

Yazıcı, Ş., İnan, G., & Tabak, V. (2007). Effect of aspect ratio and volume fraction of steel fiber on the mechanical properties of SFRC. *Construction and Building Materials*, *21*(6), 1250-1253, http://doi.org/10.1016/j.conbuildmat.2006.05.025.

Zhang, Y. Z., Wang, Q. H., Zhou, M., Fang, Y. F., & Zhang, Z. K. (2020). Mechanical properties of concrete with coarse spontaneous combustion gangue aggregate (SCGA): experimental investigation and prediction methodology. *Construction and Building Materials*, *255*, 119337, https://doi.org/10.1016/j.conbuildmat.2020.119337.

Zhu, H., Yang, S., Li, W., Li, Z., Fan, J., & Shen, Z. (2020). Study of mechanical properties and durability of alkali-activated coal gangue-slag concrete. *Materials, 13(23)*, 5576, https://doi.org/10.3390/ma13235576.